

Reference-Based Autoencoder for Surface Defect Detection

Wei Luo, *Student Member, IEEE*, Haiming Yao, *Student Member, IEEE*, Wenyong Yu, *Member, IEEE*,
and Xue Wang, *Senior Member, IEEE*

Abstract—Due to the extreme imbalance in the number of normal data and abnormal data, visual anomaly detection is important for the development of industrial automatic product quality inspection. Unsupervised methods based on reconstruction and embedding have been widely studied for anomaly detection, of which reconstruction-based methods are the most popular. However, establishing a unified model for textured surface defect detection remains a challenge because these surfaces can vary in homogeneous and non regularly ways. Furthermore, existing reconstruction-based methods do not have a strong ability to convert the defect feature to the normal feature. To address these challenges, we propose a novel unsupervised reference-based autoencoder (RB-AE) to accurately inspect a variety of textured defects. Unlike most reconstruction-based methods, artificial defects and a novel pixel-level discrimination loss function are utilized for training to enable the model to obtain pixel-level discrimination ability. First, the RB-AE employs an encoding module to extract multi-scale features of the textured surface. Subsequently, a novel reference-based attention module (RBAM) is proposed to convert the defect features to normal features to suppress the reconstruction of defects. In addition, RBAM can also effectively suppress the defective feature residual caused by skip-connection. Next, a decoding module utilizes the repaired features to reconstruct the normal texture background. Finally, a novel multiscale feature discrimination module (MSFDM) is employed to defect detection and segmentation. In addition, a two-stage train strategy is utilized to improve inspection performance. The proposed RB-AE method achieves the state-of-the-art performance on the MVTec AD dataset, with the area under the receiver operating characteristic curve (ROCAUC) of 98.81% for anomaly detection and 98.54% for anomaly segmentation over all 5 textured surface categories.

Index Terms—Texture defect inspection, reference-based feature repair, background reconstruction, multi scale feature discrimination, anomaly detection.

I. INTRODUCTION

IN THE field of manufacturing industry, surface defects commonly appear in many industrial products, such as steel [1], wood [2], and thin-film transistor liquid crystal displays (TFT-LCD) [3], because of the raw materials employed and complex manufacturing process. These defects are localized destruction of the texture surface structure or texture surface

pattern, which not only directly affects the users' experiences, but also may cause some industrial accidents. Therefore, to achieve product quality management and improve users' experience, surface defect detection has become an indispensable component during the manufacturing process.

In recent years, various surface defect detection methods have been proposed. These methods can be broadly divided into two main categories: conventional methods and deep learning-based methods. Most conventional methods [4]–[6] utilize handcrafted features to obtain texture defect representations, resulting in low inspection efficiency, high false detection rate, and poor consistency on different texture surfaces. However, as a data-driven method, deep learning-based methods can automatically extract features by training a large quantity of data, with powerful feature extraction capability and good robustness.

In the field of automatic visual inspection, deep learning-based methods can be categorized as supervised and unsupervised methods based on whether the training data contain labeled defective samples. Supervised methods require a large number of labeled defect samples to train a deep neural network. A pyramid feature fusion and global context attention network for defect segmentation were proposed in PGA-Net [7]. RetinaNet [8] proposed a deep neural network with difference channel attention and adaptively spatial feature fusion for steel surface defect detection. Although supervised methods have achieved accomplishments in the field of surface defect detection, collecting a comprehensive and balanced set of defective samples is still the main challenge when it comes to the surface defect detection problem because the number of defect-free samples is much larger than that of defective samples in the actual industrial field.

In contrast, the unsupervised methods are expected to solve the problem, because it only requires unlabeled defect-free samples for training. In recent years, embedding [9]–[11] and reconstruction [12]–[14] based methods have been studied for unsupervised anomaly detection and segmentation. Embedding-based methods detect anomalies by mapping the image to the feature domain. The Patch-SVDD framework [9] builds the embedded feature domain by leveraging self-supervised learning. The Sub-Image Anomaly Detection with Deep Pyramid Correspondences (SPADE) [10] method presents an adequate performance on anomaly detection. The Gaussian Clustering of Pretrained Feature (GCPF) [11] method leverages multiple independent Gaussian clustering to inspect anomalies. These methods can perform image-level anomaly detection, but not accurate pixel-level anomaly

Manuscript received XX XX, 20XX; revised XX XX, 20XX. This study was financially supported by the National Natural Science Foundation of China (Grant No. 51775214) (Corresponding author: Wenyong Yu.)

Wei Luo and Wenyong Yu are with the School of Mechanical Science and Engineering, Huazhong University of Science and Technology, Wuhan 430074, China (e-mail: u201910709@hust.edu.cn, ywy@hust.edu.cn).

Haiming Yao and Xue Wang are with the State Key Laboratory of Precision Measurement Technology and Instruments, Department of Precision Instrument, Tsinghua University, Beijing 100084, China (e-mail: yhm22@mails.tsinghua.edu.cn, wangxue@mail.tsinghua.edu.cn).

detection. Reconstruction-based methods apply the deep convolutional neural network (DCNN) to reconstruct the anomaly image to a normal image by restoring the anomalies. Consequently, the anomalous regions are obtained by the difference between the original input and the reconstructed one. The AnoGAN [12] utilizes the generator of a generative adversarial network to reconstruct the background. Mei *et al.* [13] propose a multiscale convolutional denoising autoencoder (MSCDAE) to inspect texture defects using only defect-free samples for model training. Yang *et al.* [14] propose a multiscale feature-clustering-based fully convolutional autoencoder (MSFCAE) method for various types of texture defect detection. These methods can't convert the defective feature to a normal feature, which leads to the reconstruction of defects. In addition, these methods do not have the pixel-level normal/anomaly discriminatory capability.

Aiming at the above challenges, we propose a novel method based on reconstruction called reference-based autoencoder (RB-AE) for the accurate detection and segmentation of various textured defects. Unlike mainstream reconstruction-based methods, artificial defects and a novel pixel-level discrimination loss function are applied to enable the model to obtain the pixel-level normal/anomaly discriminatory capability. First, an encoder module extracts multi-scale discriminable features. Consequently, a novel reference-based attention module (RBAM) is proposed to address defective features. In addition, RBAM can also effectively suppress the defective feature residual generated by skip-connection. Next, a decoder module utilizes the repaired features to reconstruct the normal background. Finally, instead of using a pixel gap between original images and reconstructed images, we propose a novel multi scale feature discrimination module (MSFDM) for more accurate defect segmentation.

The main contributions of our work are as follows:

- We propose a novel pixel-level discrimination loss function, which enables the model to obtain the pixel-level normal/anomaly discriminatory capability.
- We propose a novel reference-based attention module (RBAM), which not only repairs the defective features but also suppresses the residual of defective features caused by skip-connection.
- We propose a novel multi scale feature discrimination module (MSFDM) to segment defects more accurately.
- The proposed method achieves improved performance on the anomaly detection results on MVTec AD dataset [15] compared with the state-of-the-art methods, with the area under the receiver operating characteristic curve (ROCAUC) of 98.81% for anomaly detection and 98.54% for anomaly segmentation over all 5 textured surface categories.

The remainder of this article is organized as follows. The related work about unsupervised methods for defect detection and segmentation are stated in section II. The proposed RB-AE is introduced in detail in section III. Section IV conducts extensive experiments to analyze the performance of RB-AE. Finally, The conclusion and future work are discussed in section V.

II. RELATE WORKS

In this section, we introduce related works about unsupervised methods for defect detection and segmentation. The unsupervised methods for defect detection and segmentation can be mainly divided into two categories: embedding-based and reconstruction-based methods.

A. Embedding-based Methods

The key to embedding-based methods is to construct a well- discriminative embedding feature domain, where the abnormal images are embedded far away from the normal clusters. Recently, the pre-trained DCNN has been applied as an effective and discriminative embedding function. The CNN_Dict method [16] utilizes the pre-trained ResNet18 [17] to extract the patch-level features of the normal image, which are decomposed using the PCA [18] method and clustered into several centers using the k-means [19] clustering method. The distances of the testing features to the clustering centers are computed as the anomaly scores. Bergmann *et al.* [20] propose a Student-Teacher framework to inspect defects by the predictive uncertainty of the student network and the regression errors. The Patch SVDD [9] method is proposed to locate defects by leveraging self-supervised learning, but the extraction and retrieval of the patch-level feature are time-consuming. The SPADE [10] method utilizes K-NN [21] algorithm to retrieve similar features from the pre-stored normal features in the testing phase, which shows an effective performance on anomaly detection. Similar to the Patch-SVDD method, the two retrievals required by the SPADE method consume much more computation time and online memory storage. The GCPF [11] method is proposed to inspect defects using multiple independent Gaussian clustering, which effectively saves computation time and online memory storage. The above embedding-based methods either require much more computation time and memory storage or can't segment anomalies accurately.

B. Reconstructed-based Methods

Reconstruction-based methods have been considerably studied for defect detection and segmentation. Reconstruction-based methods utilize only defect-free images for training and are expected to restore the defects during the testing phase, and then the differences between the original images and their reconstructed images are computed to locate the defects. Auto Encoder (AE) [22] is a typical reconstruction-based method. Images reconstructed by AE are almost blurred and lack structural information. Therefore, the structural similarity [23] loss function is applied to improve the vanilla AE. Meanwhile, the vanilla AE has strong generalization capability, resulting in the reconstruction of anomalies. The MemAE [24] method proposes a memory module to mitigate the drawback of over-generation. Luo *et al.* [25] propose a clear memory-augmented autoencoder (CMA-AE) to make the model both have strong normal background reconstruction and abnormal foreground restoration ability. Recently, perceptual distance [26] demonstrates that deep features can measure the similarity

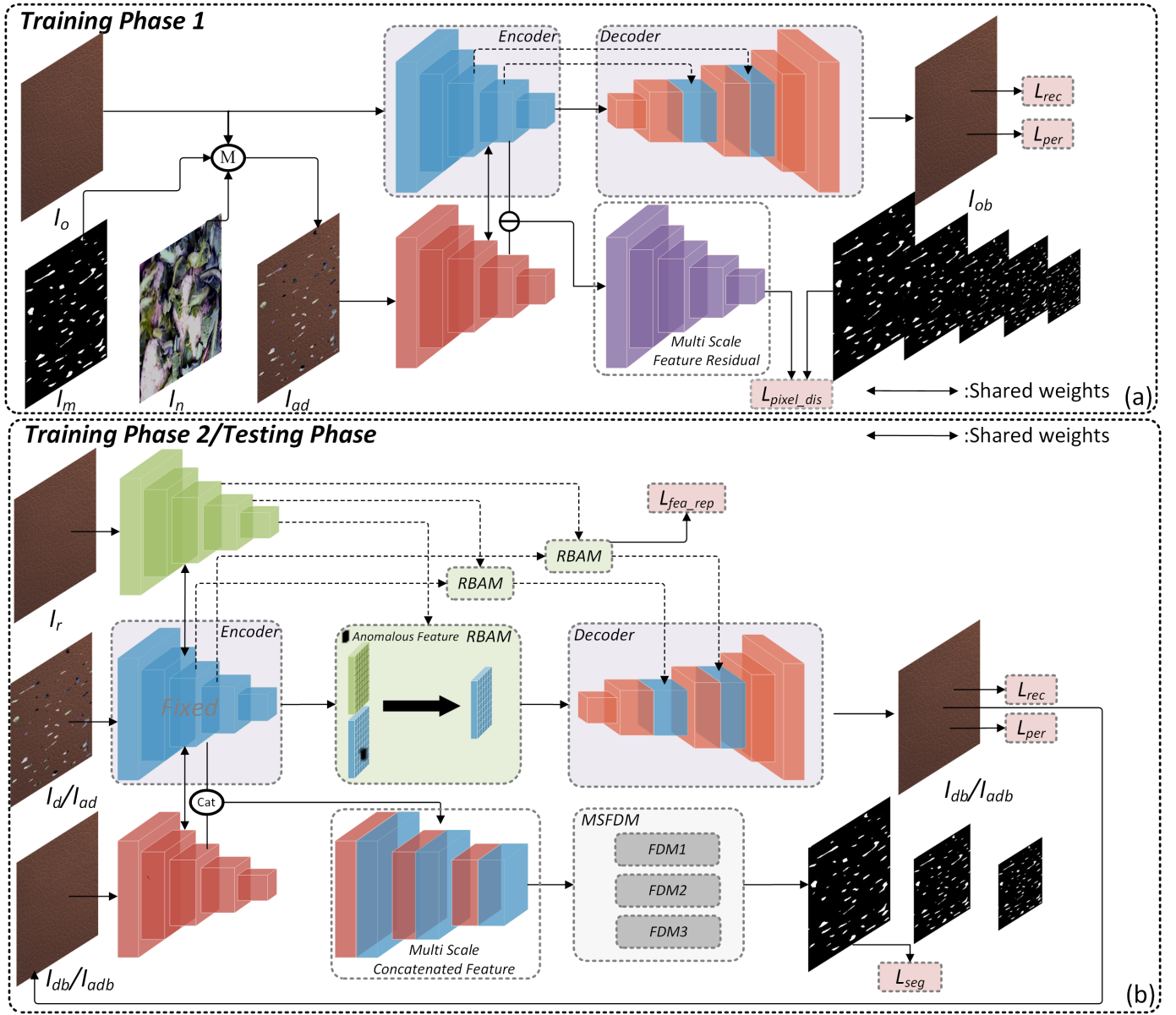


Fig. 1. Overall architecture of the proposed RB-AE methods. RB-AE consists of an encoder, a RBAM, a decoder and a MSFDM. During training phase 1, Defect-free images and artificial defect images are propagated forward. Artificial defect images and the pixel-level discrimination loss (L_{pixel_dis}) are adopted to make the encoder have pixel_level normal/abnormal discrimination ability. During training phase 2, the fixed reference defect-free image and artificial defect images are propagated forward and the weights of encoder are fixed. The RBAM utilizes the features of the fixed reference image to repair the features of artificial defect images, then the repaired features are fed or concatenated to the corresponding layers in the decoder. The MSFDM leverages the concatenated features of original artificial defect images and corresponding reconstructed images for defect segmentation. The pink boxes indicate losses.

between two images in a way that coincides with human judgment. The TrustMAE [27] method combines the MemAE and the perceptual distance for defect segmentation. The RIAD [28] method randomly removes partial patches of different sizes and reconstructs the missing information from partial inpaintings. Recently, GANs [29] have shown outstanding generative ability. the AnoGAN [12] leverages the generator of GANs to inspect defects. However, The AnoGAN and original GANs lack the mapping from the image domain to the feature domain. To settle this problem, many GAN-based methods have been proposed. The GANomaly [30] method proposes an encoder-decoder-encoder framework to optimize the model

in both image space and feature space. To achieve a more detailed reconstruction and speed up the convergence of the model, The Skip-GANomaly [31] combines the GANomaly and the skip-connection. However, the above methods can't convert defective features to normal features. The AFEAN [32] propose a global context feature editing module to eliminate the effect of defect reconstruction. The defective feature residual caused by skip-connection still exists in AFEAN and Skip-GANomaly. To address the problem, the FMR-Net [33] utilizes memory-generated features to repair the defective features. Then the repaired features are fed into the decoder through skip-connection. But the key point that FMR-Net misses is

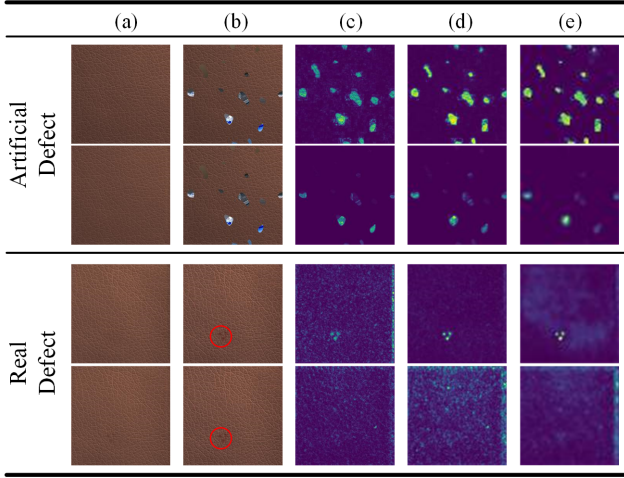


Fig. 2. Examples of the effect of the pixel-level discrimination loss function. The first row is the result of the encoder trained using L_{pixel_dis} , and the second row is the result of the traditional encoder. For artificial defects, (a) defect-free image. (b) artificial defective image. For real defect, (a) reconstructed image. (b) real defective image. (c) the feature residual of 1st layer of the encoder. (d) the feature residual of 2nd layer of the encoder. (e) the feature residual of 3rd layer of the encoder. The above real defective image is from MVTec AD dataset [15].

that the memory-generated features may also contain defective features.

Overall, how to convert defective features to normal features is still a challenge for reconstruction-based methods. To address the challenge, the RB-AE framework is proposed in this article. The RB-AE learns to repair defective features through the novel RBAM. Thus, RB-AE can reconstruct the defective images to the normal images, thereby achieving the state-of-the-art performance in defect detection and segmentation.

III. THE PROPOSED RB-AE FRAMEWORK

In this section, the proposed RB-AE framework is introduced in detail. First, the overall architecture of RB-AE is introduced briefly. Then, its main modules, including the encoder with pixel-level discriminatory capability, the reference-based attention module (RBAM), and the multiscale feature discrimination module (MSFDM), are presented in detail. Finally, the training and testing procedures of RB-AE are introduced.

A. Overall Architecture of RB-AE

The key point of the reconstruction-based methods is to convert defective features to normal features. The current reconstruction-based methods do not have strong defect repair capability. Meanwhile, they also lack pixel-level normal/abnormal discriminatory capabilities. In this study, the novel RB-AE method is proposed to address these challenges.

The overall architecture of RB-AE is shown in Fig. 1. RBAE consists of four modules: Encoder (for extracting multi-scale semantic features from images), RBAM (for repairing defects in the feature domain), Decoder (for reconstructing normal texture background from features), and MSFDM (for defect segmentation). The training procedure is divided into

two phases. In the first phase, the artificial defect images and the defect-free images are fed into the encoder. The pixel-level discrimination loss function (L_{pixel_dis}) is leveraged to make the encoder have the pixel-level normal/abnormal discriminatory ability. Then, only the features of defect-free images are fed into the decoder to reconstruct the textured background. In the second phase, the weights of the encoder are fixed and the encoder extract features of the fixed reference image and artificial defect images. The RBAM utilizes the features of the reference image to repair the features of artificial defect images. Then, the repaired features are fed into the decoder to reconstruct the textured background. Then, the reconstructed images and the original artificial defect images are re-input into the encoder and the features of the first three layers are concatenated together separately. At last, MSFDM employs concatenated features to obtain multi-scale defect segmentation maps. The procedure for the testing phase is consistent with the second training phase.

B. Encoder with Pixel-Level Normal/Abnormal Discrimination Capability

The traditional encoder is used to compress the image information and it is trained with only defect-free images. Consequently, this encoder is not capable of discriminating normal/abnormal at the pixel level. To address this challenge, we adopt pairs of images: a defect-free image I_o and its artificial defective image I_{ad} . The artificial defects are generated in a similar way to DRAEM [34]. As shown in Fig. 1(a), the artificial defective images are generated by combining the defect-free images I_o , the natural images I_n from ImageNet dataset [35] and random masks I_m :

$$I_{ad} = I_o \odot (1 - I_m) + I_n \odot I_m \quad (1)$$

where \odot denotes the dot product operation, $I_o, I_m, I_n, I_{ad} \in R^{H \times W \times C}$ and H, W, and C represent the height, width, and number of channels, respectively. Moreover, as shown in Fig. 1, we propose a novel pixel-level discrimination loss function to make the encoder the ability to discriminate normal/abnormal regions at the pixel level. Let $\Phi_l \in R^{H_l \times W_l \times C_l}$ represent the features extracted from the l th layer of the encoder. The pixel-level discrimination loss function is defined as:

$$L_{pixel_dis} = \frac{1}{L} \sum_{l=1}^L \left\| N(M(\|\Phi_l(I_o) - \Phi_l(I_{ad})\|^2)) - I_m^l \right\|^2 \quad (2)$$

where I_m^l represents the random mask resized to (H_l, W_l) , L represents the number of layers in the encoder, $M(\cdot)$ represents the mean operation at the channel dimension and $N(\cdot)$ represents the normalization operation. The effect of L_{pixel_dis} is shown in Fig. 2. As we can see, the L_{pixel_dis} indeed makes the encoder equipped with the capability of pixel-level normal/abnormal discrimination and this capability can be generalized to real defects.

C. Reference-Based Attention Module

The mainstream reconstruction-based methods can't address the defective features, resulting in the reconstruction of

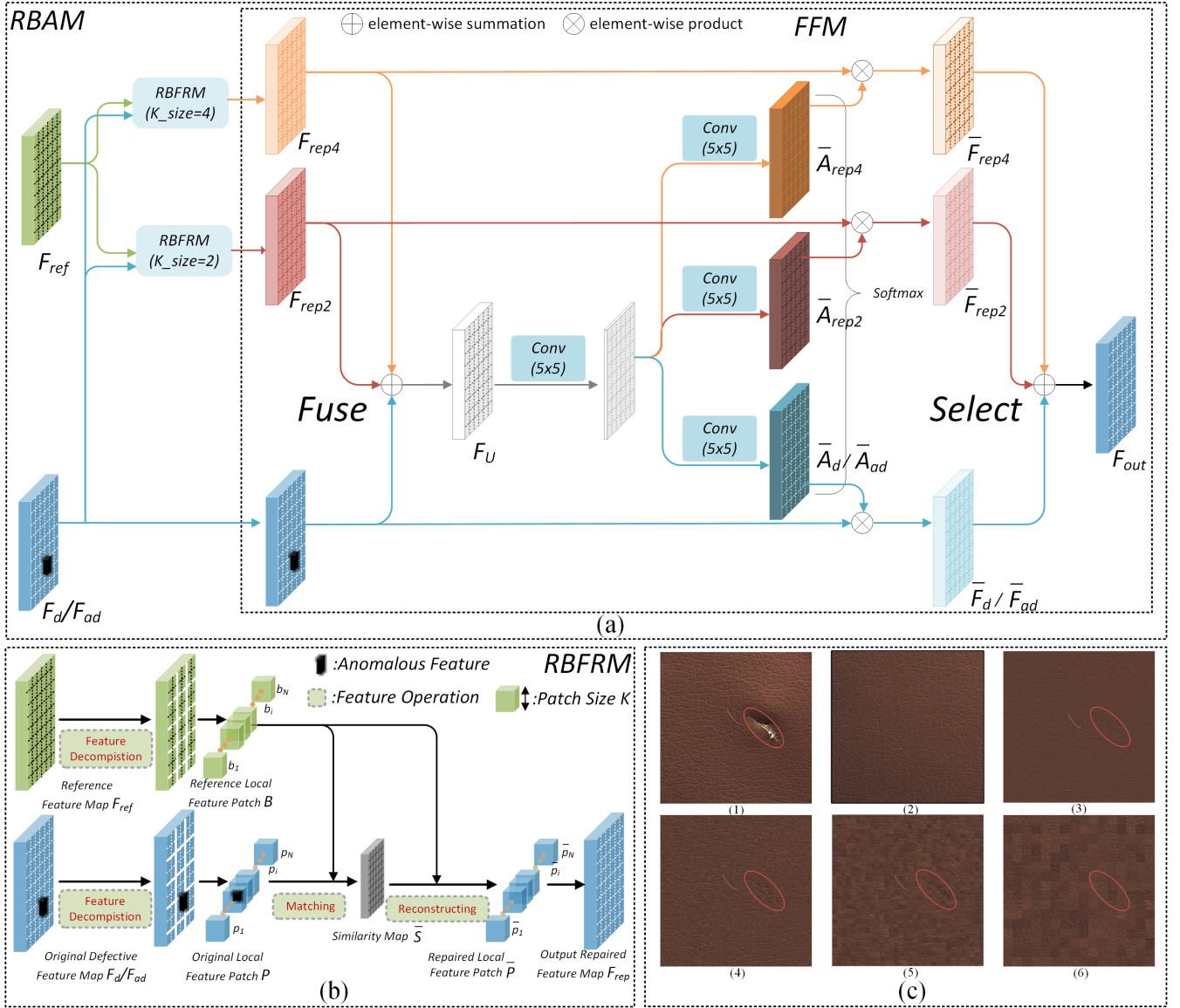


Fig. 3. (a) Architecture of the RBAM. The RBAM consists of two modules: RBFRM and FFM. (b) Illustration of the RBFRM. The RBFRM utilizes the reference features to repair the defective features. (c) Effect of patch size K on RBFRM at the image level. (1) Defective image. (2) Fixed reference defect-free image. (3) Repaired image using RBFRM whose K is 2. (4) Repaired image using RBFRM whose K is 4. (5) Repaired image using RBFRM whose K is 8. (6) Repaired image using RBFRM whose K is 16. The orange dotted lines indicate the textures. The red ellipses indicate the defects.

defects. Moreover, some methods adopt the skip-connection operation to pursue more detailed information but this brings defective features from the encoder into the decoder. To address the above problems, inspired by the contextual attention [36], RBAM is proposed to convert the defective features to normal features and suppress the defective feature residuals in skip-connection. As shown in Fig. 3 (a), the RBAM consists of the reference-based feature repair module (RBFRM) and the feature fusion module (FFM). The RBFRM and FFM are described in detail as follows.

1) *Reference-Based Feature Repair Module*: How to deal with the defective feature is a major challenge in defect detection. The FMR-Net [33] method leverages memory-generated features to repair defective features. However, the feature maps generated by memory mechanisms [24] may

also contain defective features. Therefore, we choose a fixed reference defect-free image to repair defects. As shown in Fig. 3 (b), we name the feature maps of the fixed reference defect-free image extracted by the encoder as reference feature map and denote them as $F_{ref} \in R^{H_F \times W_F \times C_F}$, where H_F , W_F and C_F represent the height, width and the number of channels, respectively, of the feature maps. Then, we divide the reference feature map into non-overlapping patches, which are named reference local feature patches and are denoted by $B = \{b_1, b_2, \dots, b_N\}$, where $b_i \in R^{K \times K \times C_F}$, $i \in (1, \dots, \frac{H_F}{K} \times \frac{W_F}{K})$ and K is the patch size. Similarly, we denote the original real/artificial defective feature map by F_d/F_{ad} and apply the same feature decomposition operation described above for a set of original local feature patches $P = \{p_1, p_2, \dots, p_N\}$, where the size of p_i is the same as

the b_i . To match the defective patches with reference defect-free patches, we calculate the cosine similarity between them as:

$$S_{i,j} = \left\langle \frac{p_i}{\|p_i\|}, \frac{b_j}{\|b_j\|} \right\rangle \quad (3)$$

where $\|\cdot\|$ represents the modulus of a tensor and $S_{i,j}$ represents the similarity map S at location (i, j) , which calculates the similarity of i th original defective feature patch and j th reference feature patch. Then, we apply the softmax function to get the normalized similarity:

$$\bar{S}_{i,j} = \frac{\exp(S_{i,j})}{\sum_{j=1}^N \exp(S_{i,j})} \quad (4)$$

Finally, we utilize the reference local feature patches B and the normalized similarity map \bar{S} to reconstruct the output repaired local feature patches $\bar{P} = \{\bar{p}_1, \bar{p}_2, \dots, \bar{p}_N\}$, described as follows:

$$\bar{p}_i = \sum_{j=1}^N b_j \cdot \bar{S}_{i,j} \quad (5)$$

Then, we obtain the output repaired feature map F_{rep} by directly composing all the repaired local feature patches.

2) *Feature Fusion Module*: The hyper-parameter patch size K of RBFRM influences the quality of feature repair. As shown in Fig. 3 (c), the larger the patch size K , the better the defective features are suppressed. However, as K increases, the repaired features retain less of the original textured features and gradually appear "checkerboard" effect. To address this problem, inspired by the SKNet [37], we propose the feature fusion module (FFM).

The architecture of the FFM is shown in Fig. 3 (a). We denote the feature map repaired by RBFRM whose K is set to 4 as F_{rep4} and F_{rep2} is defined similarly. First, we fuse the information of F_d , F_{rep2} and F_{rep4} via an element-wise summation:

$$F_U = F_d + F_{rep2} + F_{rep4} \quad (6)$$

Then we compress the channel dimension to 64 by using convolution operation with a $m \times m$ kernel, whose aim is to obtain more important channel information. Next, the three different $m \times m$ convolution kernels are applied to get attention maps \bar{A}_{rep4} , \bar{A}_{rep2} and \bar{A}_d/\bar{A}_{ad} . We assume that the size of m should be larger than the maximum K . In this paper, the maximum K is set to 4 as mentioned above, thus the m is set to 5. Specifically, we apply a softmax function on the channel-wise digits for the normalized attention maps:

$$\begin{aligned} \bar{A}_{rep4}^{i,j,k} &= \frac{\exp(A_{rep4}^{i,j,k})}{\exp(A_{rep4}^{i,j,k}) + \exp(A_{rep2}^{i,j,k}) + \exp(A_{ad}^{i,j,k})}, \\ \bar{A}_{rep2}^{i,j,k} &= \frac{\exp(A_{rep2}^{i,j,k})}{\exp(A_{rep4}^{i,j,k}) + \exp(A_{rep2}^{i,j,k}) + \exp(A_{ad}^{i,j,k})}, \\ \bar{A}_{ad}^{i,j,k} &= \frac{\exp(A_{ad}^{i,j,k})}{\exp(A_{rep4}^{i,j,k}) + \exp(A_{rep2}^{i,j,k}) + \exp(A_{ad}^{i,j,k})} \end{aligned} \quad (7)$$

where $\bar{A}_{rep4}^{i,j,k}$, $\bar{A}_{rep2}^{i,j,k}$ and $\bar{A}_{ad}^{i,j,k}$ represent the i th row, j th column, k th element of \bar{A}_{rep4} , \bar{A}_{rep2} and \bar{A}_{ad} , respectively. It

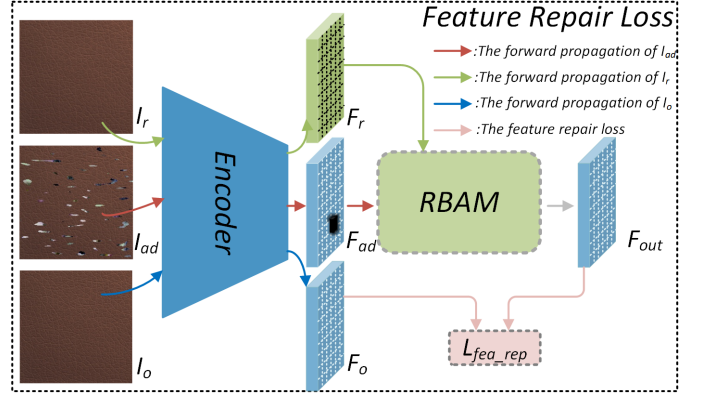


Fig. 4. Schematic of feature repair loss function. The feature repair loss function is utilized to guide the RBAM learning to repair defective features.

is obvious that $\bar{A}_{rep4} + \bar{A}_{rep2} + \bar{A}_{ad} = 1$. The three normalized attention maps are employed to select the information of F_{rep4} , F_{rep2} , and F_{ad} . Finally the output feature map F_{out} can be calculated as follows:

$$F_o = \bar{A}_{rep4} \odot F_{rep4} + \bar{A}_{rep2} \odot F_{rep2} + \bar{A}_{ad} \odot F_{ad} \quad (8)$$

where \odot denotes the dot product operation.

3) *Feature Repair Loss Function*: To guide the RBAM learn to convert the defective features to the normal features, the feature repair loss function L_{fea_rep} is proposed. As shown in Fig. 4, we can obtain the feature map of the original defect-free image, which is denoted as F_o . There is no doubt that we hope that the artificial defective feature map F_{ad} can be repaired to the corresponding original defect-free feature map F_o . Therefore, we simply calculate the mean squared error between F_o and F_{ad} as the feature repair loss function:

$$L_{fea_rep} = \frac{1}{l_2 - l_1} \sum_{l=l_1}^{l_2} \|F_{out}^l - F_o^l\|^2 \quad (9)$$

where F_o^l denotes F_o extracted by the l th layer of the encoder, likewise F_{out}^l , and l_1 and l_2 represent the first and last layer where the RBAM module is embedded into the encoder, respectively. Next, we discuss the values of l_1 and l_2 .

4) *Discussion about How the RBAMs are Embedded onto the Different Scales of RB-AE*: There are five layers of the encoder. As we all know, with the deeper encoder layer, the receptive fields of the feature maps becomes larger and the feature maps become more semantic but less detailed. There is no doubt that the local feature patches require high level semantic representation. In addition, more texture detail information can be useful for the network to reconstruct background accurately. Therefore, we need to balance the semantic representation and texture detail information. In this paper, we employ the RBAMs in the three deepest layers of RB-AE, which can obtain a good balance between the semantic representation and the texture detail information. So, the l_1 and l_2 are set to 3 and 5.

Finally, as shown in Fig. 5, the RBAM can not only suppress the defective features but also retain the normal texture features, which is useful to achieve more accurate texture background reconstruction.

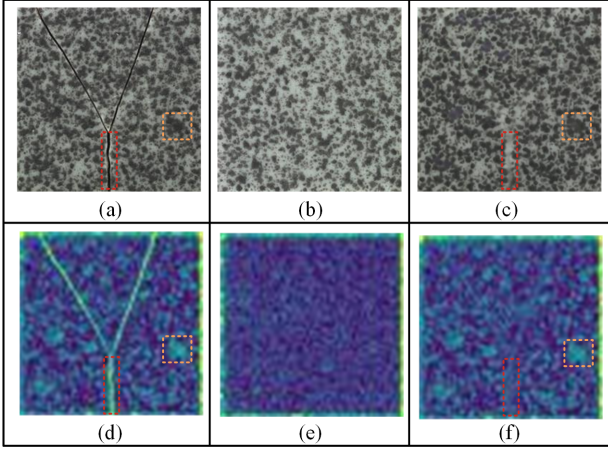


Fig. 5. Effect of the RBAM. The orange dotted boxes indicate the textures. The red dotted boxes indicate the defects. (a) the defective image. (b) the fixed reference defect-free image. (c) the reconstructed image. (d) the feature map of the defective image extracted by the 3rd layer of the encoder. (e) the feature map of the fixed reference defect-free image extracted by the 3rd layer of the encoder. (f) the output repaired feature map. The above defective image is from MVtec AD dataset [15].

D. Multi Scale Feature Discrimination Module

For the defect detection task, there are two important issues, one is how to convert the defective features to normal textured features and thus suppress the reconstruction of defects, and the other is how to accurately inspect and segment defects through the original defective images and the corresponding reconstructed images. The former can be solved by RBAM proposed above, while the latter is still a challenge. The pixel difference between the original image and its reconstructed image is commonly used for defect detection and segmentation, but there are two critical problems in this methods. The first is that individual pixel has no semantic information but discriminating normal/abnormal is based on rich contextual information. The second is that the size of industrial defects in reality is multi-scale thus achieving accurate defect detection and segmentation requires multi-scale information. To solve the two problems in pixel difference method, the multi scale feature discrimination module (MSFDM) is proposed.

As shown in Fig. 6, the MSFDM has three sub-networks, namely FDM1, FDM2 and FDM3, which are used to detect the defective features at different scales. First, the artificial/real defective image (I_{ad}/I_d) and the corresponding reconstructed image (I_{adb}/I_{db}) are re-fed into the encoder to obtain the multi-scale concatenated features $MS-C_F = \{C_{F1}, C_{F2}, C_{F3}\}$, where C_{F1} , C_{F2} and C_{F3} are the corresponding concatenated feature extracted by the first three layer of the encoder respectively. Then, the MSFDM utilizes the $MS-C_F$ to get the anomaly maps $AM = \{AM_1, AM_2, AM_3\}$ at different scales. In addition, to increase the robustness of MSFDM, we apply the Focal Loss as the segmentation loss:

$$L_{seg} = \frac{1}{3} \sum_{i=1}^3 Loss_{focal}(I_m^i, AM_i) \quad (10)$$

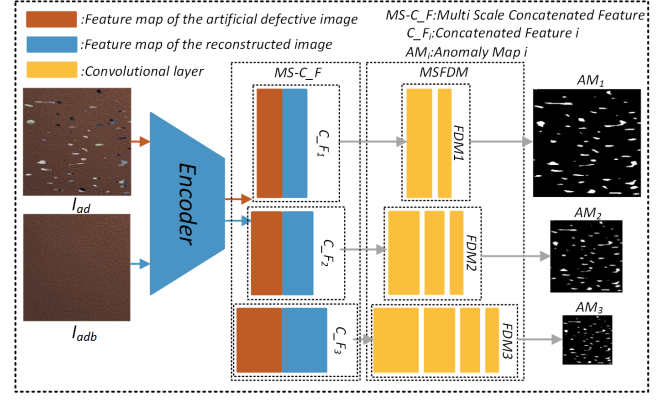


Fig. 6. Schematic of the Multi Scale Feature Discrimination Module (MSFDM).

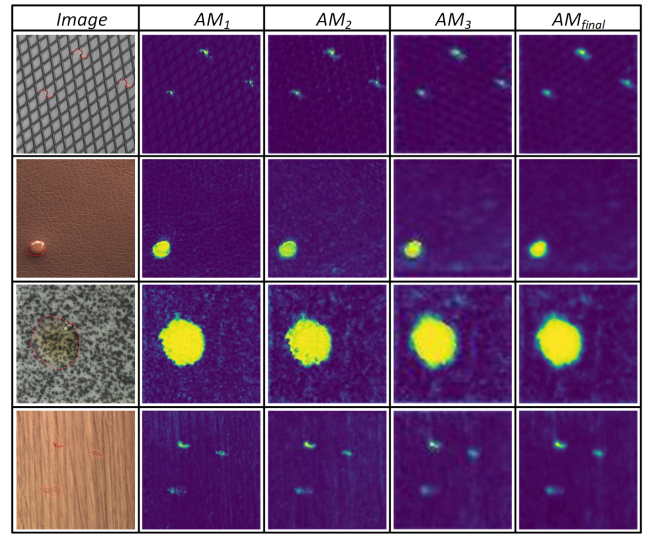


Fig. 7. Visualization results of the Multi Scale Feature Discrimination Module (MSFDM). All the above defective images are from MVtec AD dataset [15].

where I_m^i represents the random mask resized to the shape of AM_i .

Finally, some examples of the multi scale anomaly maps handled by the MSFDM module have been shown in Fig. 7. As we can see, the anomaly maps at different scales have the different discriminability for the defects. The AM_1 can capture more details of defects, but at the same time, it has a lot of noise. The AM_3 has a stronger discriminability for the defects thus it has less noise but lacks detailed information of defects such as edges. Therefore, we apply the weighted sum of the anomaly maps at different scales to obtain the final anomaly map AM_{final} :

$$AM_{final} = \lambda_1 AM_1 + \lambda_2 g(AM_2) + \lambda_3 g(AM_3) \quad (11)$$

where $g(\cdot)$ denotes a bilinear up-sampling function that resizes the anomaly map to the size of input image, λ_1 , λ_2 and λ_3 are the corresponding weights. In this paper, they are set as $\lambda_1=0.2$, $\lambda_2=0.2$, $\lambda_3=0.6$.

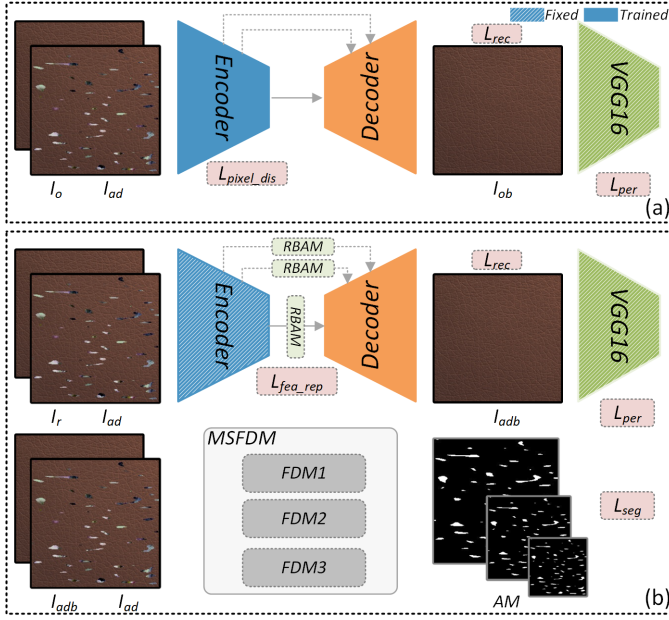


Fig. 8. Illustration of the training and testing procedures of RB-AE. (a) Training phase 1. (b) Training phase 2. The testing procedure of RB-AE is the same as training phase 2.

E. Training and Testing Procedures

To make the RB-AE has both normal/abnormal discriminability and defect repair capability, a two-phase training strategy is applied to optimize the entire model.

As shown in Fig. 8 (a), the learning targets for training phase 1 are background reconstruction and pixel-level normal/abnormal discriminability in the encoder. During training phase 1, only encoder and decoder are optimized. For texture background reconstruction, the purpose of loss function is to minimize the distance between the input image and corresponding reconstructed image. Therefore, we simply use the mean square errors as the reconstruction loss:

$$L_{rec}^1 = \mathbb{E}_{I_o \sim P_{I_o}} [\|I_o - I_{ob}\|^2] \quad (12)$$

where $\|\cdot\|^2$ denotes the L_2 norm.

To capture the high-level semantic information, the perceptual loss L_{per}^1 is leveraged by calculating the L_1 distance between the feature maps of I_o and I_{ob} :

$$L_{per}^1 = \mathbb{E}_{I_o \sim P_{I_o}} \left[\frac{1}{L} \sum_{l=1}^L \|D_l(I_o) - D_l(I_{ob})\|_1 \right] \quad (13)$$

where D_l denotes the l th feature map from ImageNet-pretrained VGG-16 backbone. We utilize the first five feature maps from the ReLU activation layers thus L is set to 5.

As mentioned in Section III-B, the encoder is trained with pixel-level discrimination loss L_{pixel_dis} to enable the model with pixel-level normal/abnormal discriminability.

We can obtain the weighted joint loss for training phase 1 by combining Eqs. (2), (12) and (13):

$$L_{phase1} = w_{rec}^1 L_{rec}^1 + w_{per}^1 L_{per}^1 + w_{pixel_dis}^1 L_{pixel_dis} \quad (14)$$

TABLE I
DETAILS OF THE DATASET

	Dataset	Carpet	Grid	Leather	Tile	Wood
Training	Abnormal	0	0	0	0	0
	Normal	280	264	245	230	247
Testing	Abnormal	88	57	72	84	60
	Normal	21	21	32	33	19

where w_{rec}^1 , w_{per}^1 and $w_{pixel_dis}^1$ are the weights of the three type of losses, and we empirically set $w_{rec}^1=100$, $w_{per}^1=1$ and $w_{pixel_dis}^1=1$. After the accomplishment of training phase 1, the model is equipped with strong background reconstruction and pixel-level discrimination ability.

As shown in Fig. 8 (b), in order not to affect the discriminability, the weights of encoder are no longer updated. The learning targets for training phase 2 are defect restoration and accurate defect segmentation. During training phase 2, the RBAM, the decoder and the MSFDM are optimized together. For defect restoration, the purpose of loss function is to minimize the distance between the reconstructed image (I_{adb}) of artificial defect and the the source defect-free image (I_o). In addition, the perceptual loss is also applied for generating the reconstructed images that are more in line with human perception. Thus, the L_{rec}^2 and L_{per}^2 are defined as:

$$L_{rec}^2 = \mathbb{E}_{I_o \sim P_{I_o}} [\|I_o - I_{adb}\|^2] \quad (15)$$

$$L_{per}^2 = \mathbb{E}_{I_o \sim P_{I_o}} \left[\frac{1}{L} \sum_{l=1}^L \|D_l(I_o) - D_l(I_{adb})\|_1 \right] \quad (16)$$

As mentioned in Section III-C, the feature repair loss (L_{fea_rep}) is utilized to guide the RBAM to learn how to convert the defective features to normal features.

For accurate defect segmentation, as mentioned in Section III-D, the segmentation loss (L_{seg}) is leveraged to improve the robustness of MSFDM.

With the combination of Eqs. (9), (10), (15) and (16), the weighted joint loss function for training phase 2 can be defined as:

$$L_{phase2} = w_{rec}^2 L_{rec}^2 + w_{per}^2 L_{per}^2 + w_{fea_rep}^2 L_{fea_rep} + w_{seg}^2 L_{seg} \quad (17)$$

where w_{rec}^2 , w_{per}^2 , $w_{fea_rep}^2$ and w_{seg}^2 are the weights of the four type of losses, and they are set as $w_{rec}^2=100$, $w_{per}^2=1$, $w_{fea_rep}^2=1$ and $w_{seg}^2=1$. After the accomplishment of training phase 2, the RB-AE model can achieve accurate surface defect detection.

During testing procedure, similar to training phase 2, when the defective image is fed, the RB-AE model can address the defective features to suppress the reconstruction of defects. Then, the input defective image and the defect-free reconstructed image are re-input to encoder to obtain multi scale concatenated features. Finally, MSFDM utilizes the multi scale concatenated features to obtain the final anomaly map.

IV. EXPERIMENTAL RESULTS

To evaluate the performance of the proposed RB-AE method, a series of experiments are conducted in this section.

TABLE II
THE IMAGE LEVEL ROCAUC RESULTS OF DIFFERENT SOTA METHODS ON FIVE TYPES OF TEXTURES IN MVTEC AD DATASET

Category	Reconstruction-based methods							Embedding-based methods			RB-AE
	AE_SSIM	AnoGAN	f-AnoGAN	GANomaly	VAE	TrustMAE	RIAD	MKD	SPADE	Pacth SVDD	
Carpet	67.00	49.00	56.57	84.20	67.00	97.43	84.20	79.30	92.80	92.90	<u>95.41</u>
Grid	69.00	51.00	59.63	74.30	83.00	99.08	99.60	78.10	47.30	94.60	<u>99.37</u>
Leather	46.00	52.00	62.50	79.20	71.00	95.07	100.00	95.10	<u>95.40</u>	90.90	100.00
Tile	52.00	51.00	61.34	78.50	81.00	97.29	98.70	91.60	<u>96.50</u>	97.80	99.44
Wood	83.00	68.00	75.00	65.30	89.00	99.82	93.00	94.30	95.80	<u>96.50</u>	99.82
Average	64.40	52.20	63.01	76.30	78.20	<u>97.74</u>	95.10	87.68	85.56	94.54	98.81

¹ The best image level ROCAUC performance is indicated by bold font, while the second best is indicated by an underline.

TABLE III
THE PIXEL LEVEL ROCAUC RESULTS OF DIFFERENT SOTA METHODS ON FIVE TYPES OF TEXTURES IN MVTEC AD DATASET

Category	Reconstruction-based methods					Embedding-based methods					RB-AE
	AE_SSIM	AnoGAN	VAE	TrustMAE	RIAD	MKD	SPADE	DFR	GCPF	Pacth SVDD	
Carpet	87.00	54.00	73.50	98.53	96.30	95.60	97.50	97.00	98.90	92.60	97.62
Grid	94.00	58.00	96.10	97.45	98.80	91.80	93.70	98.00	97.80	96.20	98.50
Leather	78.00	64.00	92.50	98.05	99.40	98.10	97.60	98.00	99.30	97.40	99.43
Tile	59.00	50.00	65.40	82.48	89.10	82.80	87.40	87.00	96.10	91.40	99.52
Wood	73.00	62.00	83.80	92.62	85.80	84.80	88.50	94.00	<u>95.10</u>	90.80	97.64
Average	78.00	58.00	82.26	93.83	93.70	90.62	92.94	94.80	<u>97.44</u>	93.68	98.54

¹ The best pixel level ROCAUC performance is indicated by bold font, while the second best is indicated by an underline.

TABLE IV
THE PROAUC RESULTS OF DIFFERENT SOTA METHODS ON FIVE TYPES OF TEXTURES IN MVTEC AD DATASET

Category	Reconstruction-based methods				Embedding-based methods						RB-AE
	AE_SSIM	AnoGAN	VAE	EdgRec	SPADE	CNN_Dict	ST	MB-PFM	PaDiM	STPM	
Carpet	64.70	20.40	50.10	96.90	94.70	46.90	87.90	96.90	96.20	95.80	93.20
Grid	84.90	22.60	22.40	97.00	86.70	18.30	95.20	96.00	<u>94.60</u>	<u>96.60</u>	95.72
Leather	56.10	37.80	63.50	98.80	97.20	64.10	94.50	98.80	97.80	98.00	98.79
Tile	17.50	17.70	87.00	<u>96.30</u>	75.90	79.70	94.60	88.70	86.00	92.10	97.39
Wood	60.50	38.60	62.80	<u>77.50</u>	87.40	62.10	91.10	92.60	91.10	93.60	93.55
Average	56.74	27.42	57.16	93.30	88.38	54.22	92.70	94.60	93.14	<u>95.22</u>	95.73

¹ The best PROAUC performance is indicated by bold font, while the second best is indicated by an underline.

First, the datasets and implementation details are introduced. Second, the overall detection performance of RB-AE is compared with that of several state-of-the-art methods. Third, the ablation study is conducted to illustrate the influence of each module in the RB-AE, including L_{pixel_dis} , RBAM and MSFDM. At last, the industrial application of RB-AE is introduced.

A. Datasets and Implementation Details

1) *Datasets*: The MVTEC AD dataset [15] have been widely used for unsupervised defect detection and segmentation, which consists of 5 types of textures: carpet, grid, leather, tile and wood. A total of 1266 defect-free texture images and no defective images are given for training. There are 126 defect-free images and 361 defective images for testing. The texture defects in the testing images are variant in color, scale, shape and etc, which make MVTEC AD very challenging. In our experiments, each images is resized into the resolution of 256×256. The more details of the datasets are summarized in TABLE I.

2) *Implementation Details and Evaluation Criterion*: All experiments are implemented on a computer with Xeon(R) Silver 4116 CPU@2.10GHz and NVIDIA V100 GPU with 32GB memory size. The entire RB-AE model is optimized using the Adam optimizer with a learning rate of 0.0001 and

a weight decay of 0.00001. The training epoch sizes for the two-phase training procedure are set to 400 and 200.

The key of fairly comparing the performance of each method is evaluation criterion. In this paper, we follows the area under the receiver operating characteristic curve (ROCAUC) for detection and segmentation, which is commonly used as the evaluation metric in unsupervised anomaly detection. However, the ROCAUC for segmentation favors large defective areas, which leads to the inaccurate evaluation. Thus, we also adopt the normalized area under the per-region overlap curve (PROAUC) as the defect segmentation evaluation criterion.

B. Overall Comparative Experiments with the RB-AE

To verify the performance of the proposed RB-AE method, the inspection performance of RB-AE is compared with the long-standing reconstruction-based methods AE_SSIM [38], f-AnoGAN [39], AnoGAN [12], GANomaly [30], VAE [40], TrustMAE [27], RIAD [28], EdgRec [41], and the embedding-base methods MKD [42], CNN_Dict [16], SPADE [10], DFR [43], GCPF [11], Patch SVDD [9], ST [20], MB-PFM [44], PaDiM [45], STPM [46].

1) *Defect Detection*: As shown in TABLE II, the proposed RB-AE achieves better defect detection performance than that

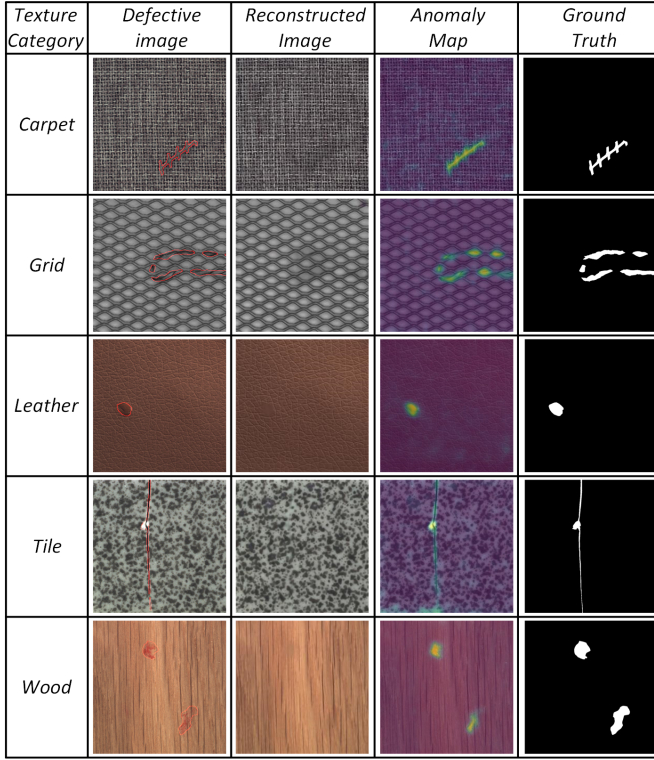


Fig. 9. Reconstruction and segmentation results on the various texture images. All the above defective images are from MVTec AD dataset [15].

of other state-of-the-art methods. AE_SSIM, AnoGAN and f-AnoGAN do not perform well. Although RIAD, TrustMAE and Patch SVDD perform better, they are unable to maintain good inspection performance for all texture categories. For example, RIAD achieves the outstanding performance on Leather with image level ROCAUC of 100.00%, but the poor performance on Carpet with image level ROCAUC of 84.20%. In contrast, our proposed RB-AE can perform well for all categories. This is because the L_{pixel_dis} makes the extracted features more discriminative, then MSFDM utilize these more discriminative features to detect the defects easily.

2) *Defect Segmentation*: As shown in TABLE III, the RB-AE also achieves better defect segmentation performance compared with other outstanding methods. Especially for the Tile and Wood, the RB-AE improves the pixel level ROCAUC by margins of 3.42% and 2.54% compared to the second best results. This demonstrates that the RB-AE can detect defects well at pixel level. However, due to that the pixel ROCAUC favors the large defective areas which may lead to inaccurate evaluation for defect segmentation, the PROAUC criterion is also utilized to evaluate the performance of defect segmentation. As shown in TABLE IV, the RB-AE achieves the better average result overall texture categories on defect segmentation. Compared to the second best reconstruction-based method, the RB-AE improves the PROAUC by margins of 2.43%. This is because RBAM can suppress the reconstruction of defects well and thus we can obtain defect-free reconstruction images, which contributes to more accurate defect localization.

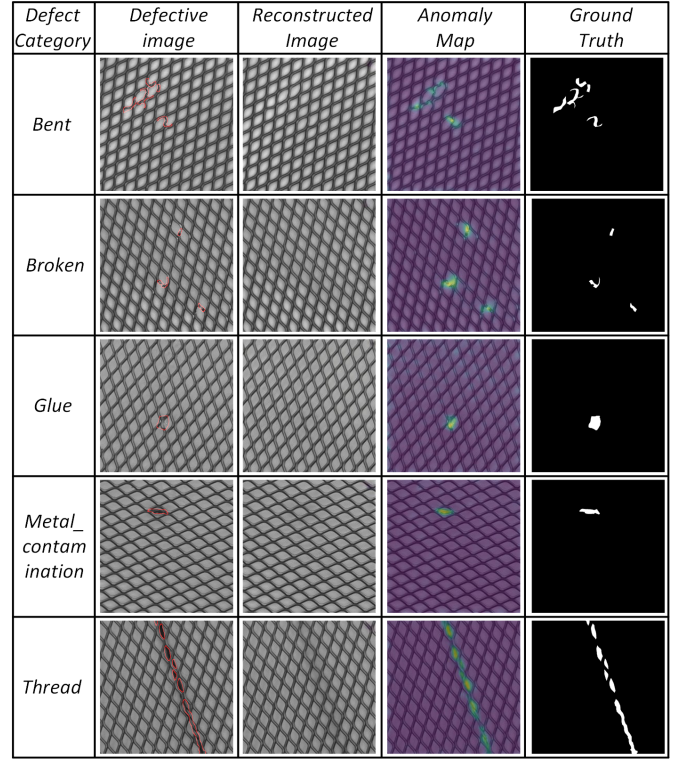


Fig. 10. Reconstruction and segmentation results on the various types of defects. All the above defective images are from MVTec AD dataset [15].

Some detection results of RB-AE on the five types of texture images are shown in Fig. 9. As we can see, RB-AE not only can reconstruct the normal texture background and repair the defects but also achieve accurate defect segmentation on all types of texture surfaces. In addition, as shown in Fig. 10, the RB-AE is also capable of inspecting the various types of defects accurately, such as bent, broken, glue, metal_contamination and thread.

C. Ablation Study of the RB-AE

In this subsection, to analysis the effectiveness of each component of RB-AE, a series of ablation experiments are conducted on the wood dataset. In particular, we compare MSFDM with other segmentation methods, such as pixel gap between input images and corresponding reconstructed images, multi scale feature residual (MSFR) [25] and structure similarity index measure (SSIM) [23]. To guarantee a fair comparison, the parameter settings of all the variants of RB-AE are kept the same. The qualitative and quantitative experimental results are shown in Fig. 11 and TABLE V respectively.

1) *Influence of L_{pixel_dis}* : L_{pixel_dis} is a novel loss function, making it possible for the model to discriminate normal/abnormal at the pixel level. The more discriminative features contribute to the more accurate defect detection and segmentation. Thus, the influence of the L_{pixel_dis} is analyzed in detail.

Column C of Fig. 11 shows the examples of the influence of L_{pixel_dis} . The anomaly maps obtained by the model without

TABLE V
RB-AE ABLATION STUDY ON THE WOOD DATASET

Module	A	B	C	D	E	F
Encoder	✓	✓	✓	✓	✓	✓
RBAM	✓		✓	✓	✓	✓
L_{pixel_dis}	✓	✓		✓	✓	✓
Decoder	✓	✓	✓	✓	✓	✓
MSFDM	✓	✓	✓			
Pixel Gap				✓		
MSFR					✓	
SSIM						✓
Image ROCAUC	99.82	98.58	98.77	97.06	98.16	91.23
Pixel ROCAUC	97.64	96.73	95.22	84.35	92.36	86.45

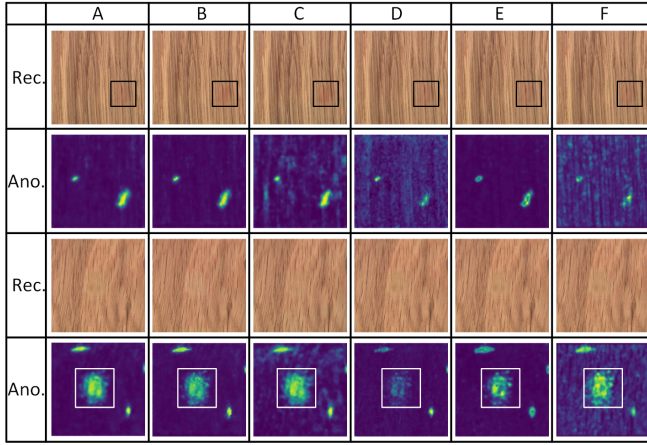


Fig. 11. Examples of images from tests in the ablation study. Rec. denotes the reconstructed image, and Ano. denotes the anomaly map.

the L_{pixel_dis} have more noise. This is because the model without the L_{pixel_dis} can't discriminate the defects at the pixel level. The quantitative results are described in column C of TABLE V. When the RB-AE is trained without L_{pixel_dis} , the image/pixel ROCAUC values decrease by 1.05/2.42% compared to the entire RB-AE (column A).

These experimental results demonstrate that the L_{pixel_dis} can improve the overall inspection performance. Leveraging the L_{pixel_dis} to train makes the model have the ability of distinguishing the normal/abnormal at the pixel level, which benefits the defect detection and segmentation.

2) *Influence of RBAM*: The RBAM aims to leverage the reference normal features to repair the defective features, resulting in defect-free reconstructed images, which is the basis for subsequent defect segmentation. Therefore, the influence of RBAM is studied in detail.

The examples of the influence of RBAM are shown in column B of Fig. 11. Compared with the entire RB-AE, the RB-AE without RBAM can't address the defective features well, which leads to misinspection. The quantitative results of RB-AE without RBAM are shown in column B of TABLE V. When the RBAM is removed, the image/pixel ROCAUC values decrease by 1.24/0.91% compared to the entire RB-AE (column A).

These experimental results verify that the RBAM can improve the ability of addressing defects. Using the reference features to repair the defective features, the model can obtain more clear reconstructed images, which is helpful to achieve more accurate defect segmentation.

3) *Influence of MSFDM*: The MSFDM is used to segment the defects through the input images and corresponding reconstructed images, which is the key to achieve accurate defect segmentation. Thus, the MSFDM is compared with pixel gap, MSFR and SSIM segmentation methods.

Column D, E and F of Fig. 11 show the examples of the influence of MSFDM. The MSFDM can obtain more clear anomaly detection compared to pixel gap (column D) and SSIM (column F). Compare with the MSFR (column E), the MSFDM can achieve more accurate defect localization. The quantitative results are shown in column D, E and F of TABLE V. When the MSFDM is replaced with pixel gap, MSFR and SSIM, the image/pixel ROCAUC values decrease by 2.76/13.29%, 1.66/5.28% and 8.59/11.19% respectively compared to the entire RB-AE (column A).

These experimental results demonstrate that the MSFDM is superior to other segmentation methods. MSFDM leverages the multi scale concatenated discriminative features to segment defects, which further improve the overall performance.

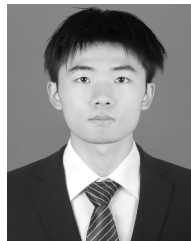
V. CONCLUSION

In this article, an unsupervised RB-AE method is proposed for accurate defect detection and segmentation. This method is only trained on defect-free images and corresponding artificial defective images. First, the L_{pixel_dis} is leveraged to make the feature extracted by the encoder more discriminative at the pixel level. In addition, a novel RBAM is proposed to suppress the reconstruction of defects, which leverages the normal feature of the fixed reference defect-free image to repair the defective feature. Then, the decoder utilizes the repaired features reconstruct the texture background. Next, the reconstructed images and the original input images are re-fed into the encoder to obtain multi scale concatenated features. Finally, the MSFDM utilizes the multi scale concatenated features to detect and segment defects accurately. The proposed RB-AE achieves better inspection performance on defect detection and segmentation compared with the long-standing methods on MVTec AD dataset. However, due to the diversity of object, the RB-AE can only be applied for defect detection on texture surfaces. In follow-up research, we will focus on how to apply this method to object surfaces.

REFERENCES

- [1] H. Wang, J. Zhang, Y. Tian, H. Chen, H. Sun, and K. Liu, "A simple guidance template-based defect detection method for strip steel surfaces," *IEEE Transactions on Industrial Informatics*, 2019. 1
- [2] O. Silven, M. Niskanen, and H. Kauppinen, "Wood inspection with non-supervised clustering," *machine vision applications*, 2003. 1
- [3] H. Yang, K. Song, S. Mei, and Z. Yin, "An accurate mura defect vision inspection method using outlier-prejudging-based image background construction and region-gradient-based level set," *IEEE Transactions on Automation Science and Engineering*, 2018. 1
- [4] D. Aiger and H. Talbot, "The phase only transform for unsupervised surface defect detection," *computer vision and pattern recognition*, 2010. 1

- [5] D.-M. Tsai and T.-Y. Huang, "Automated surface inspection for statistical textures," *Image and Vision Computing*, 2003.
- [6] X. Xianghua and M. Mirmehdi, "Texems: Texture exemplars for defect detection on random textured surfaces," *IEEE Transactions on Pattern Analysis and Machine Intelligence*, 2007. I
- [7] H. Dong, K. Song, Y. He, J. Xu, Y. Yan, and Q. Meng, "Pga-net: Pyramid feature fusion and global context attention network for automated surface defect detection," *IEEE Transactions on Industrial Informatics*, 2020. I
- [8] X. Cheng and J. Yu, "Retinanet with difference channel attention and adaptively spatial feature fusion for steel surface defect detection," *IEEE Transactions on Instrumentation and Measurement*, 2021. I
- [9] J. Yi and S. Yoon, "Patch svdd: Patch-level svdd for anomaly detection and segmentation," *asian conference on computer vision*, 2020. I, II-A, IV-B
- [10] T. Reiss, N. Cohen, L. Bergman, and Y. Hoshen, "Panda: Adapting pretrained features for anomaly detection and segmentation," *computer vision and pattern recognition*, 2020. I, II-A, IV-B
- [11] Q. Wan, L. Gao, X. Li, and L. Wen, "Industrial image anomaly localization based on gaussian clustering of pre-trained feature," *IEEE Transactions on Industrial Electronics*, 2021. I, II-A, IV-B
- [12] T. Schlegl, P. Seeböck, S. M. Waldstein, U. Schmidt-Erfurth, and G. Langs, "Unsupervised anomaly detection with generative adversarial networks to guide marker discovery," *information processing in medical imaging*, 2017. I, II-B, IV-B
- [13] S. Mei, H. Yang, and Z. Yin, "An unsupervised-learning-based approach for automated defect inspection on textured surfaces," *IEEE Transactions on Instrumentation and Measurement*, 2018. I
- [14] H. Yang, Y. Chen, K. Song, and Z. Yin, "Multiscale feature-clustering-based fully convolutional autoencoder for fast accurate visual inspection of texture surface defects," *IEEE Transactions on Automation Science and Engineering*, 2019. I
- [15] P. Bergmann, M. Fauser, D. Sattlegger, and C. Steger, "Mvtec ad — a comprehensive real-world dataset for unsupervised anomaly detection," *computer vision and pattern recognition*, 2019. I, 2, 5, 7, IV-A1, 9, 10
- [16] P. Napolitano, F. Piccoli, and R. Schettini, "Anomaly detection in nanofibrous materials by cnn-based self-similarity," *Sensors*, 2018. II-A, IV-B
- [17] K. He, X. Zhang, S. Ren, and J. Sun, "Identity mappings in deep residual networks," *european conference on computer vision*, 2016. II-A
- [18] M. E. Tipping and C. M. Bishop, "Probabilistic principal component analysis," *Journal of The Royal Statistical Society Series B-statistical Methodology*, 1999. II-A
- [19] J. A. Hartigan and M. A. Wong, "Algorithm as 136: A k-means clustering algorithm," *Journal of the royal statistical society. series c (applied statistics)*, vol. 28, no. 1, pp. 100–108, 1979. II-A
- [20] P. Bergmann, M. Fauser, D. Sattlegger, and C. Steger, "Uninformed students: Student-teacher anomaly detection with discriminative latent embeddings," *computer vision and pattern recognition*, 2019. II-A, IV-B
- [21] L. E. Peterson, "K-nearest neighbor," *Scholarpedia*, vol. 4, no. 2, p. 1883, 2009. II-A
- [22] G. E. Hinton and R. Salakhutdinov, "Reducing the dimensionality of data with neural networks," *Science*, 2006. II-B
- [23] Z. Wang, A. C. Bovik, H. R. Sheikh, and E. P. Simoncelli, "Image quality assessment: from error visibility to structural similarity," *IEEE Transactions on Image Processing*, 2004. II-B, IV-C
- [24] D. Gong, L. Liu, V. Le, B. Saha, M. R. Mansour, S. Venkatesh, and A. van den Hengel, "Memorizing normality to detect anomaly: Memory-augmented deep autoencoder for unsupervised anomaly detection," *international conference on computer vision*, 2019. II-B, III-C1
- [25] W. Luo, T. Niu, L. Tang, W. Yu, and B. Li, "Clear memory-augmented auto-encoder for surface defect detection," *arXiv preprint arXiv:2208.03879*, 2022. II-B, IV-C
- [26] R. Zhang, P. Isola, A. A. Efros, E. Shechtman, and O. Wang, "The unreasonable effectiveness of deep features as a perceptual metric," *computer vision and pattern recognition*, 2018. II-B
- [27] D. S. Tan, Y.-C. Chen, T. P.-C. Chen, and W.-C. Chen, "Trustmae: A noise-resilient defect classification framework using memory-augmented auto-encoders with trust regions," *workshop on applications of computer vision*, 2021. II-B, IV-B
- [28] V. Zavrtanik, M. Kristan, and D. Skočaj, "Reconstruction by inpainting for visual anomaly detection," *Pattern Recognition*, vol. 112, p. 107706, 2021. II-B, IV-B
- [29] I. Goodfellow, J. Pouget-Abadie, M. Mirza, B. Xu, D. Warde-Farley, S. Ozair, A. Courville, and Y. Bengio, "Generative adversarial nets," *neural information processing systems*, 2014. II-B
- [30] S. Akcay, A. Atapour-Abarghouei, and T. P. Breckon, "Ganomaly: Semi-supervised anomaly detection via adversarial training," *asian conference on computer vision*, 2018. II-B, IV-B
- [31] S. Akçay, A. Atapour-Abarghouei, and T. P. Breckon, "Skip-ganomaly: Skip connected and adversarially trained encoder-decoder anomaly detection," in *2019 International Joint Conference on Neural Networks (IJCNN)*. IEEE, 2019, pp. 1–8. II-B
- [32] H. Yang, Q. Zhou, K. Song, and Z. Yin, "An anomaly feature-editing-based adversarial network for texture defect visual inspection," *IEEE Transactions on Industrial Informatics*, 2021. II-B
- [33] H. Yao, W. Yu, and X. Wang, "A feature memory rearrangement network for visual inspection of textured surface defects toward edge intelligent manufacturing," *IEEE Transactions on Automation Science and Engineering*, 2022. II-B, III-C1
- [34] V. Zavrtanik, M. Kristan, and D. Skočaj, "Draem-a discriminatively trained reconstruction embedding for surface anomaly detection," in *Proceedings of the IEEE/CVF International Conference on Computer Vision*, 2021, pp. 8330–8339. III-B
- [35] O. Russakovsky, J. Deng, H. Su, J. Krause, S. Satheesh, S. Ma, Z. Huang, A. Karpathy, A. Khosla, M. S. Bernstein, A. C. Berg, and L. Fei-Fei, "Imagenet large scale visual recognition challenge," *International Journal of Computer Vision*, 2014. III-B
- [36] J. Yu, Z. Lin, J. Yang, X. Shen, X. Lu, and T. S. Huang, "Generative image inpainting with contextual attention," in *Proceedings of the IEEE conference on computer vision and pattern recognition*, 2018, pp. 5505–5514. III-C
- [37] X. Li, W. Wang, X. Hu, and J. Yang, "Selective kernel networks," *computer vision and pattern recognition*, 2019. III-C2
- [38] P. Bergmann, S. Löwe, M. Fauser, D. Sattlegger, and C. Steger, "Improving unsupervised defect segmentation by applying structural similarity to autoencoders," *arXiv preprint arXiv:1807.02011*, 2018. IV-B
- [39] T. Schlegl, P. Seeböck, S. M. Waldstein, G. Langs, and U. Schmidt-Erfurth, "f-anogan: Fast unsupervised anomaly detection with generative adversarial networks," *Medical image analysis*, vol. 54, pp. 30–44, 2019. IV-B
- [40] D. Dehaene, O. Frigo, S. Combexelle, and P. Eline, "Iterative energy-based projection on a normal data manifold for anomaly localization," in *International Conference on Learning Representations*, 2019. IV-B
- [41] T. Liu, B. Li, Z. Zhao, X. Du, B. Jiang, and L. Geng, "Reconstruction from edge image combined with color and gradient difference for industrial surface anomaly detection," *arXiv preprint arXiv:2210.14485*, 2022. IV-B
- [42] M. Salehi, N. Sadjadi, S. Baselizadeh, M. H. Rohban, and H. R. Rabiee, "Multiresolution knowledge distillation for anomaly detection," in *Proceedings of the IEEE/CVF conference on computer vision and pattern recognition*, 2021, pp. 14902–14912. IV-B
- [43] Y. Shi, J. Yang, and Z. Qi, "Unsupervised anomaly segmentation via deep feature reconstruction," *Neurocomputing*, 2021. IV-B
- [44] Q. Wan, L. Gao, X. Li, and L. Wen, "Unsupervised image anomaly detection and segmentation based on pre-trained feature mapping," *IEEE Transactions on Industrial Informatics*, 2022. IV-B
- [45] D. Thomas, S. Aleksandr, L. Angelique, and A. Romaric, "Padim: A patch distribution modeling framework for anomaly detection and localization," *Lecture Notes in Computer Science*, 2021. IV-B
- [46] G. Wang, S. Han, E. Ding, and D. Huang, "Student-teacher feature pyramid matching for unsupervised anomaly detection," *arXiv: Computer Vision and Pattern Recognition*, 2021. IV-B



Wei Luo will receive the B.S. degree from the School of Mechanical Science and Engineering, Huazhong University of Science and Technology, Wuhan, China, in 2023. He is going to pursue a Ph.D. degree with the Department of Precision Instrument, Tsinghua University.

His research interests include deep learning, anomaly detection and machine vision.



Haiming Yao received a B.S. degree from the School of Mechanical Science and Engineering, Huazhong University of Science and Technology, Wuhan, China, in 2022. He is pursuing a Ph.D. degree with the Department of Precision Instrument, Tsinghua University.

His research interests include deep learning, edge intelligence and machine vision.



Wenyong Yu received an M.S. degree and a Ph.D. degree from Huazhong University of Science and Technology, Wuhan, China, in 1999 and 2004, respectively. He is currently an Associate Professor with the School of Mechanical Science and Engineering, Huazhong University of Science and Technology.

His research interests include machine vision, intelligent control, and image processing.



Xue Wang received an M.S. degree in measurement and instrumentation from Harbin Institute of Technology, Harbin, China, in 1991 and a Ph.D. degree in mechanical engineering from Huazhong University of Science and Technology, Wuhan, China, in 1994.

He was a Postdoctoral Fellow in electrical power systems with Huazhong University of Science and Technology from 1994 to 1996. He then joined the Department of Precision Instrument, Tsinghua University, Beijing, China, where he is currently a Professor. From May 2001 to July 2002, he was a

Visiting Professor with the Department of Mechanical Engineering, University of Wisconsin–Madison. His research interests include topics in wireless sensor networks, cyberphysical systems, intelligent biosignal processing, medical image processing, and smart energy utilization.

Prof. Wang is a senior member of the IEEE Instrumentation and Measurement Society, Computer Society, Computational Intelligence Society, and Communications Society.